The Journal of Chemical Physics ARTICLE pubs.aip.org/aip/jcp

Modeling the P3HT microcavity reflectance spectrum: Introducing a partitioning scheme for treating large disordered chromophore ensembles

Cite as: J. Chem. Phys. 163, 164125 (2025); doi: 10.1063/5.0294547
Submitted: 4 August 2025 • Accepted: 5 October 2025 •
Published Online: 29 October 2025

Hamed Haghshenas,[1] Mauricio Arias,[1] Aleesha George,[2] Andrew J. Musser,[2] Felipe Herrera,[3] and Frank C. Spano[1,a)]

AFFILIATIONS

[1] Department of Chemistry, Temple University, Philadelphia, Pennsylvania 19122, USA
[2] Department of Chemistry and Chemical Biology, Cornell University, Ithaca, New York 14853, USA
[3] Department of Physics, Universidad de Santiago de Chile, Santiago 9170124, Chile

[a)] **Author to whom correspondence should be addressed:** spano@temple.edu

ABSTRACT

Analysis of the microcavity reflectivity spectrum of a thin poly(thiophene) (P3HT) film is presented, based on the Frenkel–Holstein–Tavis–Cummings Hamiltonian and a Lindblad formalism to describe relaxation through system–bath interactions. A partitioning scheme is employed to treat large, disordered ensembles of P3HT chain segments, which, based on analysis of the free-space absorption spectrum, is divided into aggregate (60%) and amorphous (40%) domains. The reflectivity spectrum is in excellent agreement with the measured spectrum when the ensemble light–matter coupling, $\sqrt{N}g_S$, is taken to be 0.9 eV, where N is the total number of P3HT chain segments (in the aggregate and amorphous domains) and g_s is the light–matter coupling for a single segment. The spectrum exhibits a relatively narrow lower polariton (LP) feature with a much broader upper polariton (UP), with an approximate Rabi splitting of 1 eV. The two relatively weak middle polaritons are attributed to bright vibronic polaritons, which owe their spectral appearance to a Herzberg–Teller mechanism in which exciton–phonons with zero quasi-momentum borrow optical intensity from the LP and UP. The spectral feature attributed to the LP originates mainly from aggregate domains, while the UP originates from both aggregate and amorphous domains.

I. INTRODUCTION

Organic microcavities featuring molecular vibronic transitions strongly coupled to photonic modes are intensively investigated for their promising technological applications, particularly in the control of chemical reaction rates[1–10] and the enhancement of energy transport.[11–22] Such microcavities have emerged as an exceptionally rich platform where coherent and dissipative processes involving hybrid light–matter polaritonic eigenstates coexist, leading to complex spectral features observable in reflectivity, transmission, and photoluminescence (PL) measurements. Accurately capturing these features requires not only a microscopic treatment of the light–matter interaction but also a robust theoretical framework for handling dissipation.

Although most reports of organic microcavities involve small π-conjugated molecules, there have been several investigations involving conjugated polymers, such as poly(3-hexylthiophene) or P3HT.[23–25] P3HT is the most thoroughly investigated conjugated polymer for optoelectronic applications. Thin films of P3HT exhibit a semi-crystalline morphology, with π-stacked domains necessary for enhanced energy and charge transfer.[26] In organic photovoltaic devices, for example, P3HT, is often used as the absorbing material.[27] After excitation by a solar photon, the P3HT exciton effectively shuttles energy to acceptor molecules, whereupon charge-separation ensues. A recent work by DelPo *et al.*[23] showed how embedding P3HT/acceptor films in microcavities can enhance photovoltaic performance. They measured a substantial Rabi splitting of ~1 eV, which is roughly half the exciton transition energy, formally

placing P3HT microcavities in the ultra-strong coupling regime of cavity quantum electrodynamics (QED).[28] Peters *et al.*[24] showed that for a similar Rabi splitting, the rate of photodegradation for P3HT is reduced threefold inside a cavity. The most recent work by George *et al.*[25] reproduced the large Rabi splitting and further showed that the strong disorder inherent in P3HT films makes the microcavity photophysics approachable within the strong rather than the ultra-strong coupling regime. They arrived at this conclusion by modeling the disordered films with an arbitrary number of Lorentzian dipole oscillators coupled to a single cavity mode, with the oscillator frequencies and light–matter couplings fit from the free-space absorption spectrum. Their approach, which is similar to the multi-oscillator "arrowhead" Hamiltonian matrix model,[29,30] yielded a quasi-continuum of hybridized exciton–photon states beyond the usual bright/dark dichotomy.[25,31–33]

Building upon the phenomenological model of George *et al.*,[25] we present in this work an analysis of the P3HT microcavity reflectivity spectrum based on the Frenkel–Holstein–Tavis–Cummings (FHTC) Hamiltonian.[34–37] In addition to the radiation–matter coupling to a single cavity mode, the Hamiltonian includes local vibronic coupling involving a symmetric intramolecular vibration as well as excitonic coupling between chromophores. The generally complex morphology typical of polymer films is accounted for by assuming the coexistence of amorphous domains, consisting of disordered chain segments, and aggregate domains, consisting of locally ordered π-stacked chain segments.[38,39] When the Coulomb coupling is suppressed, the FHTC Hamiltonian reduces to the more popular Holstein–Tavis–Cummings (HTC) Hamiltonian[31,32,40–44] where the vibronic coupling was shown to result in the formation of bright and dark vibronic polaritons.[31,32,41]

For P3HT vibronic coupling mainly involves the aromatic-quinoidal stretching mode, which is evident in the pronounced vibronic progressions observed in the absorption spectrum of thin films. Excitonic (Coulomb) couplings between chromophores within P3HT aggregates distort the progression in a manner consistent with H-aggregation.[38,39,45–47] In order to treat the large number N of chromophores (chain segments) in a realistic sample which can potentially interact with the cavity electric field ($N \approx 10^7$–10^{10}), we expand our partition scheme, originally introduced in Ref. 48 to treat permutationally symmetric ensembles, to include site-disordered ensembles. This allows one to better treat the complex morphology inherent in P3HT films. An efficient, alternative way to deal with large molecular ensembles based on just a few chromophores was recently developed by Pérez-Sánchez *et al.*[49]

Several theoretical strategies have been developed to compute optical spectra in cavity QED systems.[50–58] A widely adopted approach is the input–output theory as formulated by Gardiner and Collett[59] and later extended to the ultra-strong coupling regime by Ciuti *et al.*[60] In this last framework, absorption and emission spectra are computed directly from the steady-state scattering response of cavity operators and offer analytical tractability for linear bosonic systems. In addition, Keeling and co-workers[44,61] adopted a linear response approach based on the power spectrum of the system operators' correlation functions using Green's function theory. Recently, Yuen-Zhou and Koner[62] provided a valuable consolidation of these previous studies, presenting them in a cohesive framework that highlights the role of molecular susceptibility in determining the linear optical response of molecular polaritons. Their framework successfully captures temperature-dependent spectral modulations arising from molecular rotations and vibrations.

In an effort to derive expressions for absorption, reflectivity, and transmission, which explicitly include the energies, ω_{Gj}, and relaxation rates, Γ_j, of the jth polariton, Herrera and Spano[31] introduced a microscopic quantum-optical model based on the HTC Hamiltonian which incorporates radiative and cavity decay processes within a Lindblad master equation framework.[33,63] The weak, monochromatic probe field was treated perturbatively, consistent with linear response theory.[31] Their formalism revealed the critical role of unusual dark vibronic polaritons, which are invisible in the cavity absorption spectrum, but nevertheless contribute to photoluminescence. Notably, in Ref. 31, spectra are computed by integrating the population-weighted power spectrum over emission frequencies, providing access to both radiative and non-radiative contributions in the cavity's output.

In this article, we extend the theoretical framework in Ref. 31 by refining the treatment of radiative observables within the Lindblad formalism[63] and applying it to simulate the optical reflectivity spectra of an organic cavity filled with a semicrystalline P3HT thin film—in particular, the system reported in the experimental study by George *et al.*[25] We begin by analyzing the free-space absorption spectrum of P3HT using a Frenkel–Holstein Hamiltonian in order to determine the relative abundance of aggregated vs amorphous regions. By incorporating the full polaritonic eigenspectrum of the FHTC Hamiltonian and explicitly modeling polariton populations including non-radiative and vibrational decay, we construct a master equation-based approach capable of reproducing and interpreting the spectral signatures observed in angle-resolved reflectivity measurements of organic cavities. To manage the computational complexity of large chromophore ensembles, we employ the aforementioned partitioning scheme, along with the simple ansatz introduced in Ref. 48. We obtain good spectral convergence with only a small number of collective chromophore states. Overall, agreement between the simulated and measured spectra both in free space and inside the cavity is excellent; this includes the energies and spectral linewidths of the lower and upper polaritons as well as the two intermediate (middle) polaritons. We show that the first middle polariton, blueshifted from the lower polariton by ~0.23 eV, can be accounted for with a Herzberg–Teller (HT) mechanism,[64,65] whereby dark exciton–phonon polaritons become bright by borrowing oscillator strength from the lower and upper polaritons. HT coupling has also been invoked to account for the enhanced emission observed in metallo-porphyrin microcavities by Rury and co-workers.[66,67] Overall, our analysis reveals the importance of vibronic coupling in the photophysics of organic microcavities.

II. THIN FILM CHARACTERIZATION

We start by modeling the UV–vis absorption spectral line shape of a P3HT thin film in free-space (outside a cavity), as obtained in a recent experimental study.[25] The spectrum is reproduced in Fig. 1 (black curve). In agreement with initial studies,[38,39] the spectrum displays a vibrational progression (A_1,A_2, A_3, …) related to the intramolecular, symmetric stretching mode, with energy $\hbar\omega_{\mathrm{vib}} = 0.174$ eV and a broad, high-energy tail. As concluded in

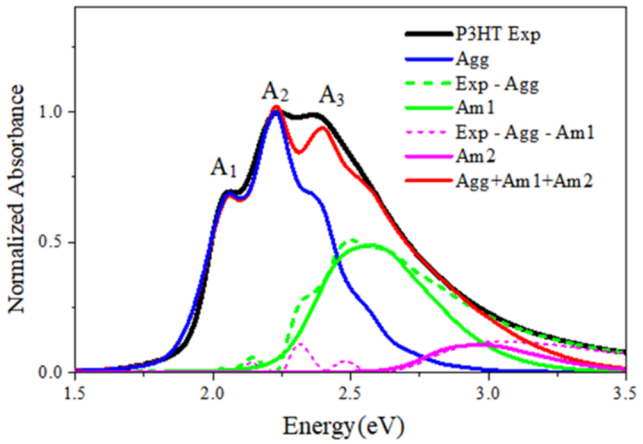

FIG. 1. Normalized experimental and simulated absorption spectra for a semi-crystalline P3HT thin film in free space. The black solid curve represents the measured spectrum from Ref. 25 taken at room temperature. The H-aggregate spectrum (blue) containing $N_A = 9$ segments was generated using the Hamiltonian in Eq. (1) (without the amorphous term), with the parameters from Table I. The contribution from the amorphous region, obtained by subtracting the aggregate spectrum from the measured spectrum (green dash), was fit with two disordered ensembles, Am1 ($N_1 = 5$) and Am2 ($N_2 = 1$) represented, respectively, by the green and magenta solid lines. The latter were obtained using the Hamiltonian in Eq. (1) (without the aggregate term) with parameters taken from Table I. In both aggregate and amorphous simulations, the HR factor was set to $\lambda^2 = 1$ and 200 configurations of disorder were averaged to obtain the spectra (see the text for additional details).

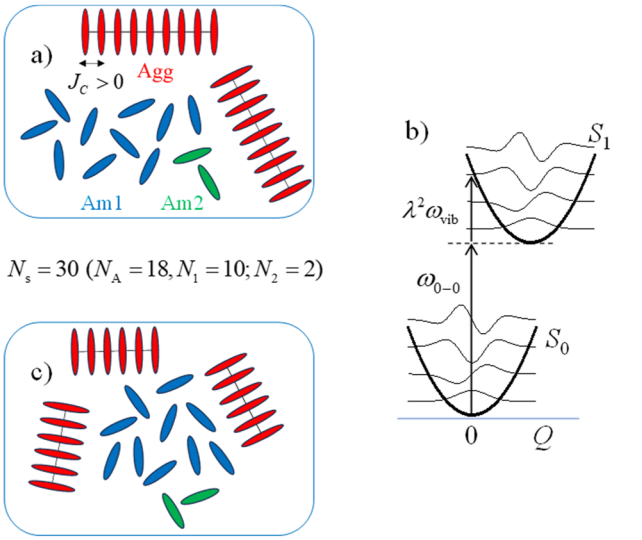

FIG. 2. (a) Segregation of semi-crystalline P3HT thin film into aggregate and amorphous regions, with the composition deduced from analysis of the absorption spectrum (see the text). Shown are a total of $N_S = 30$ segments, 18 of which are involved in H-aggregates, where the Coulomb coupling between neighboring segments is positive due to the side-by-side relative orientation. (b) Harmonic potential energy surfaces for the S_0 and S_1 states in each chromophore segment. Since the aggregate spectrum converges after four segments (see Fig. S.1) the distribution in panel (c) is essentially equivalent to panel (a) with respect to the spectral response.

Ref. 39, the vibronically structured, lower-energy region of the spectrum derives from H-aggregates comprised of π-stacked planarized P3HT segments. Within such stacks, the nearest-neighbor separation is only 0.38 nm,[68] leading to substantial Coulombic interactions by as much as 0.03 eV between neighboring chains. In Ref. 39, the higher-energy, unstructured portion of the spectrum was shown to align closely with the spectrum obtained from P3HT in solution where aggregates do not form (at sufficiently high temperature) and isolated chains are more torsionally disordered. Hence, higher-energy portion of the spectrum was attributed to the amorphous regions in thin films.

Figure 2(a) depicts the simplified aggregate/amorphous distribution used to model P3HT thin films in this work. Each of the 30 P3HT chain segments resides either in an aggregate or amorphous region. The aggregate region contains π-stacked planarized segments with nearest-neighbor Coulomb interactions, whereas amorphous regions contain isolated segments with no Coulomb interactions. As discussed in Ref. 39, each segment can be modeled with displaced harmonic potential energy surfaces representing the ground (S_0) and excited (S_1) electronic states with an associated Huang–Rhys (HR) factor of approximately unity; see Fig. 2(b). We assume for simplicity that the HR factor is the same for aggregated vs amorphous segments, but the 0–0 frequency varies considerably. For a segment within an aggregate, the 0–0 frequency has lower energy (due to enhanced planarization) and is given by $\omega_{0-0}^{Agg} = 2.02$ eV, which is slightly less than the peak A_1 shown in Fig. 1. (From here on, set $\hbar$ to unity.) In what follows, we utilize two amorphous regions in order to better describe the high energy region of the absorption spectrum beyond 2.5 eV. Since the amorphous segments have higher torsional disorder, they have substantially higher 0–0 energies, with $\omega_{0-0}^{Am1} = 2.45$ eV and $\omega_{0-0}^{Am2} = 2.85$ eV. (We emphasize that the two amorphous regions are not distinct morphological phases. They are introduced to better fit the absorption spectrum. For example, an even better fit would entail three amorphous regions.) The aforementioned 0–0 energies of the aggregate and amorphous regions as well as the relative number of aggregate vs amorphous segments are determined through detailed analysis of the absorption spectrum, as described in the following.

Figure 2(c) shows the same relative composition as Fig. 2(a) except that the aggregated segments are divided among three distinct aggregates instead of two in Fig. 2(a). Since the calculated aggregate absorption spectrum converges after just four segments (see Fig. S.1 in the supplementary material), both distributions shown in Figs. 2(a) and 2(b) yield the same absorption spectrum. For simplicity in what follows, we, therefore, assume a single aggregate containing N_A chromophores.

In order evaluate the excited states corresponding to the aggregate/amorphous distribution, we employ a Frenkel–Holstein (FH) Hamiltonian, as described in greater detail in Refs. 38, 39, and 45–47. The Frenkel–Holstein (FH) Hamiltonian (with $\hbar = 1$) takes the form

$$H_{FH} = H_{Agg} + \sum_{j=1}^{2} H_{Am,j} + H_{vib} + H_{ex-vib}. \quad (1)$$

The first three terms represent just the electronic part which differs in the three regions,

$$H_{\mathrm{Agg}} = \sum_{n=1}^{N_{\mathrm{A}}} (\omega_{0-0}^{\mathrm{Agg}} + \Delta_n^{\mathrm{Agg}})|n\rangle\langle n| + \sum_{n=1}^{N_{\mathrm{A}}} J_C\{|n\rangle\langle n+1| + h.c.\}, \quad (2)$$

$$H_{\mathrm{Am1}} = \sum_{n=N_A+1}^{N_A+N_1} (\omega_{0-0}^{\mathrm{Am\,1}} + \Delta_n^{\mathrm{Am\,1}})|n\rangle\langle n|, \quad (3)$$

$$H_{\mathrm{Am2}} = \sum_{n=N_A+N_1+1}^{N} (\omega_{0-0}^{\mathrm{Am\,2}} + \Delta_n^{\mathrm{Am\,2}})|n\rangle\langle n|. \quad (4)$$

Here, $|n\rangle$ is the pure electronic state in which the nth segment is electronically excited to the S_1 state. N_{A} is the total number of aggregated segments, and N_j is the number of segments in the jth amorphous region. The total number of chromophores is, therefore, $N = N_{\mathrm{A}} + N_1 + N_2$. Note that there is no electronic coupling between segments in different regions. This will not be the case when the film is situated between two mirrors, as each segment will then be indirectly coupled to all other segments (independent of region) through their common interaction with the enclosed cavity mode.

Disorder is accounted for by assuming an inhomogeneous distribution of site energies; the nth site in the aggregate is assigned the value Δ_n^{Agg}, which is chosen randomly from a Gaussian distribution with standard deviation, σ_{Agg}. For the jth amorphous region, the site-energy fluctuation at the nth site, $\Delta_n^{\mathrm{Am}j}$, is also distributed normally, but with a larger standard deviation, $\sigma_{A,j}$, to reflect the increasing torsional disorder. The values chosen are determined by fitting the absorption spectrum in free-space, as described in the following.

The vibrational energy due to the aromatic-quinoidal stretching mode is included in the term,

$$H_{\mathrm{vib}} = \omega_{\mathrm{vib}} \sum_{n=1}^{N} b_n^\dagger b_n, \quad (5)$$

where ω_{vib}, = 0.174 eV and the sum is over all segments, $N = N_{\mathrm{A}} + N_1 + N_2$. $b_n^\dagger$ (b_n) is the creation (annihilation) operator which creates (destroys) a vibrational quantum on the nth site relative to the unshifted harmonic well [see Fig. 2(c)]. Finally, the linear exciton–vibrational coupling, which represents the shifted on-site excited-state potential energy surface, is

$$H_{\mathrm{ex-vib}} = \omega_{\mathrm{vib}}\lambda \sum_{n=1}^{N} \{(b_n^\dagger + b_n) + \lambda\}|n\rangle\langle n|. \quad (6)$$

The HR factor, λ^2, is taken to be unity for P3HT.[38,39,46,47] As mentioned above, the vibrational energy and HR factor are assumed to be the same for every chromophore n, whether in aggregated or amorphous regions.

In order to determine the absorption spectrum corresponding to the composite aggregate/amorphous system, we first determine the eigenstates and energies of the Hamiltonian in Eq. (1), represented in a multi-particle basis set consisting of one- and two-particle states.[45,69] One particle states, $|n, \tilde{\nu}\rangle$, consist of an electronic excitation at site n with $\tilde{\nu}$ (=0, 1, 2, ...) vibrations in the shifted S_1 nuclear potential well. Two-particle states $|n, \tilde{\nu}; m, \nu\rangle$ consist of a vibronic excitation at site n and a pure vibrational excitation at site m, consisting of ν (=1, 2, ...) vibrational quanta in the unshifted ground-state nuclear potential well S_0. Two-particle states are increasingly important for obtaining accurate absorption spectra as the exciton bandwidth increases.[45] For P3HT, single-particle states are the major contributors to the states responsible for absorption, with the two-particle states contributing ~10%. (Three- and higher-particle states have negligible contributions.) After obtaining the eigenstates $|\varepsilon_j\rangle$ and eigenfrequencies ω_j, we then compute the free-space absorption spectrum using the expression,

$$A_0(\omega) = \left\langle \sum_j \frac{|\langle G|\hat{\mu}|\varepsilon_j\rangle|^2}{(\omega - \omega_j)^2 + \Gamma_{\mathrm{hom}}^2} \right\rangle_C, \quad (7)$$

where $|G\rangle$ is the electronic/vibrational ground state, in which all chromophore segments are in their ground S_0 electronic states with no vibrational quanta. The matrix element in Eq. (7) involves the dimensionless, positive frequency part of the transition dipole operator, $\hat{\mu}_{tot} = \mu_s(\hat{\mu}^\dagger + \hat{\mu})$, where μ_s is the segment transition dipole moment, and

$$\hat{\mu} \equiv \sum_n |g\rangle\langle n| = \sqrt{N}|g\rangle\langle k = 0|, \quad (8)$$

with the sum taken over all aggregated and amorphous chromophore segments. Here, the state $|k = 0\rangle$ represents the symmetric sum, $N^{-1/2}\sum|n\rangle$. Hence, absorption is only possible for eigenstates of the Hamiltonian containing at least a minimal contribution of the $|k = 0\rangle$ state. Finally, in Eq. (7), Γ_{hom} is the homogeneous linewidth, which is set to 0.03 eV in all simulations, and $\langle\cdots\rangle_C$ indicates an average over a sufficient number of configurations of disorder to obtain convergence in $A(\omega)$. We note that since Γ_{hom} is substantially smaller than the inhomogeneous linewidth, it has only a minor impact on the spectral line shape.

In what follows, we decompose the measured absorption spectrum into aggregate and amorphous contributions by adhering to the procedure originally outlined in Refs. 38 and 39. We begin with the low-energy vibronically structured region of the spectrum and fit the first two peaks A_1 and A_2 using just the aggregate portion of the Hamiltonian in Eq. (1). In P3HT H-aggregates ($J_C > 0$), the vibronic progression is distorted relative to the monomer (single segment) spectrum, with the peak intensity ratio, I_{A_1}/I_{A_2}, reduced relative to the monomer value of $1/\lambda^2 \approx 1$. When the Coulomb coupling J_C (>0) is weak compared to the vibrational energy, the peak ratio abides by the perturbative expression,[38,39,45–47]

$$\frac{I_{A_1}}{I_{A_2}} = \left(\frac{1 - 0.24W/\omega_{\mathrm{vib}}}{1 + 0.073W/\omega_{\mathrm{vib}}}\right)^2, \quad (9)$$

where the HR factor is taken to be $\lambda^2 = 1$, and $W = 4J_C$ is the free-exciton bandwidth. Reproducing the spectral ratio in the measured spectrum requires $J_C = 0.027$ eV. The blue solid line in Fig. 1 is obtained by using the aggregate-only Hamiltonian in Eq. (1) with $N_{\mathrm{A}} = 9$. To obtain the measured inhomogeneous linewidths of the A_1 and A_2 peaks, the width of the aggregate disorder distribution was set to $\sigma_{\mathrm{Agg}} = 0.06$ eV. The blue spectrum in Fig. 1 is the result of averaging over 200 configurations of disorder to ensure convergence. Although the aggregate spectrum satisfactorily accounts for the low-energy region of the experimental spectrum, it fails to capture the measured intensity beyond the A_2 peak. In

accord with Ref. 39, the higher-energy region is due to nonaggregated (amorphous) chromophores. To estimate their contribution to the spectrum, we subtract the aggregate (blue) spectrum from the measured spectrum yielding the green dashed curve shown in Fig. 1.

We next model the green dashed curve in Fig. 1 by restricting the Hamiltonian in Eq. (1) to just the amorphous 1 chromophores. Obtaining the unstructured, blueshifted spectrum requires the 0–0 peak for the amorphous 1 segments to be 2.45 eV, significantly higher than the aggregate value (2.02 eV), and an enhanced disorder width, $\sigma_{Am1} = 0.09$ eV, which is sufficient to mask the vibronic progression (after averaging over 200 configurations of disorder). With these parameters, we obtain the green solid curve in Fig. 1. Importantly, to obtain the correct oscillator strength (relative to the aggregate), we needed to include $N_1 = 5$ segments, slightly more than half the number of aggregate segments. Agreement between the green solid and dashed curves is good up to ~2.6 eV, after which the simulated amorphous 1 spectrum fails to capture the extra oscillator strength present in the green dash spectrum. To remedy this, we assume the presence of a second amorphous region, the spectrum of which is estimated by subtracting the green spectrum from the greendashed spectrum giving the dashed magenta spectrum in Fig. 1. Reproducing this spectrum requires an even higher 0–0 transition frequency of 2.85 eV, but a similar disorder width to amorphous region 1, i. e., $\sigma_{Am2} = 0.09$ eV. The solid magenta curve represents our simulation of the second amorphous region. The relatively weak oscillator strength requires only one segment in the second amorphous region, $N_2 = 1$.

Finally, the red solid curve in Fig. 1 represents the simulated spectrum based on the sum of the aggregate and amorphous spectra. The complete set of parameters is summarized in Table I. The agreement with the measured spectrum is good across a broad spectral range. The analysis shows that aggregates are dominant, accounting for 60% of the P3HT segments, followed by 33% in the first amorphous region and only 7% in the second amorphous region. We note that our sample size of only $N = 15$ segments is large enough to represent the entire ensemble. For example, doubling the size so that $N_A = 18$, $N_1 = 10$, and $N_2 = 2$ has negligible impact on the calculated spectrum. This is easy to appreciate for the amorphous regions and understandable for the aggregate as well since the spectrum for a single aggregate converges already for only four segments, as demonstrated in Fig. S.1 in the supplementary material. Hence, the 18 aggregated segments can just as well be distributed among three aggregates of six segments, each with essentially no change in the absorption spectrum.

III. CAVITY REFLECTIVITY SPECTRUM

We now consider the P3HT microcavity reflectance spectrum reported in Ref. 25 and replotted in Fig. 3 (black curve). It corresponds to an angle of 10° between the probe wave vector and the cavity axis, for which the resonant cavity mode has energy of ~2.4 eV. The spectrum displays a relatively sharp lower polariton (LP) and a much broader upper polariton (UP) with a separation (Rabi splitting) of ~1 eV. There are also two less intense "middle" polaritons, labeled MP_1 and MP_2. In what follows, we will address all such spectral features utilizing a Hamiltonian that includes radiation–matter coupling along with a partitioning scheme, which allows one to treat large numbers of chromophores in a computationally efficient manner.

Having obtained the thin film composition from the absorption spectrum analysis of Sec. II, we proceed by expanding the

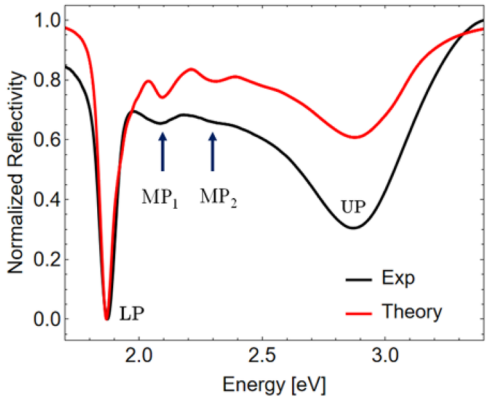

FIG. 3. Measured P3HT microcavity reflectivity spectrum from Ref. 25 (black) alongside the simulated spectrum (red). The theoretical spectrum is based on the reflectivity expression in Eq. (19) and the Hamiltonian in Eq. (10) including both one- and two-particle material excited states as well as photon-vibration states containing up to three vibrational quanta. The aggregate/amorphous composition is taken from Table I. The partitioning scheme was employed with $N_s = 30$ and 500 configurations of disorder. Additional parameters are listed in Table II.

TABLE I. Free space fitting parameters used to simulate the absorption of the P3HT semi-crystalline thin film. In addition, the vibrational frequency ω_{vib} is set to 0.174 eV (1400 cm^{-1}) and the HR factor is unity ($\lambda^2 = 1$) for aggregate and amorphous regions.

Morphology	Composition		ω_{0-0} (eV)	J_C (eV)	σ_l (eV)
Components	Percentage	N_l	0-0 transition frequency	Coulomb coupling	Standard deviation
Aggregate	60	$N_A = 9$	2.02	0.027	0.06
Amorphous 1	33	$N_1 = 5$	2.45	0	0.09
Amorphous 2	7	$N_2 = 1$	2.85	0	0.09

Frenkel–Holstein Hamiltonian in Eq. (1) to include the coupling to a single microcavity radiation mode. This results in the Frenkel–Holstein–Tavis Cummings (FHTC) Hamiltonian,[34–37]

$$H_{\mathrm{FHTC}} = H_{\mathrm{FH}} + \omega_c a^\dagger a + \frac{g_s}{2}\sum_{n=1}^{N}\{|G\rangle\langle n|a^\dagger + |n\rangle\langle G|a\}. \qquad (10)$$

Here, the cavity mode with energy ω_c is represented by the bosonic harmonic oscillator ladder operators $a^\dagger$ and a. The mode energy is represented by the second term, while the last term accounts for the light–matter interaction within the rotating wave approximation (RWA). g_S represents the coupling between the cavity mode and a single segment, which can reside within the aggregate or amorphous regions.

We acknowledge that the Rabi splitting is large enough to justify ultrastrong coupling (USC) and the use of counter-rotating terms in the light–matter interaction Hamiltonian. However, as we show in Sec. S.2 of the supplementary material (see Fig. S.2), the deviations in the Rabi splitting expected in the USC regime—as well as deviations in the LP and UP energies—are generally less than 5% over a range of cavity detunings, supporting a similar conclusion reached by George *et al.*[25] Although, the supplementary material derivation is based on the Tavis–Cummings Hamiltonian without disorder, we expect our conclusions to remain valid in the presence of exciton–vibrational coupling and inhomogeneous broadening. Indeed, theoretical evidence has shown that vacuum Rabi splitting (VRS) is enhanced when the disorder width is lower or comparable with the cavity leakage rate κ,[36] In addition, Schwennicke *et al.*,[70] showed that the presence of substantial disorder can dramatically enhance the VRS, leading to an apparent onset of the ultrastrong coupling regime.

The sum in Eq. (10) is over all N chromophores in the realistic macroscopic sample in which $N = 10^7$–10^{10}. According to the analysis in Sec. II, about 60% of such segments are involved in aggregates, while the remaining 40% is distributed over the two amorphous regions. However, we can no longer treat the three regions separately as all segments are indirectly coupled through the last term in Eq. (10). Hence, unlike the absorption spectrum shown in Fig. 1, it is not possible to view the reflectance spectrum as a sum of the aggregate and amorphous region spectra. The indirect coupling makes it necessary to include the entire ensemble of N segments, where the Rabi splitting scales as $\sqrt{N}g_s$.

A. Collective states and partitioning

The first effort is to obtain the relatively small subset of polariton eigenstates of the FHTC Hamiltonian which contribute directly to the cavity spectrum. In order to treat the large number of chromophore segments comprising a realistic sample, we expand the partition method introduced in Ref. 48 to include aggregates. We first define a "unit" as the minimal number of chromophore segments that capture the thin film composition (aggregate vs amorphous regions) as determined in Sec. II. Hence, a unit consists of 15 segments divided into nine aggregated segments, five segments in the first amorphous region and one segment in the second amorphous region. The entire sample of N chromophores is then partitioned into N_G groups with each group containing a total of N_S segments, where N_S is an integral number of units (a multiple of 15). The total number of segments in the entire sample is therefore $N = N_S \times N_G$. An example of such a partitioning scheme based on the Tavis–Cummings Hamiltonian is illustrated in Fig. 4 for a sample containing $N = 120$ chromophores divided into four groups ($N_G = 4$, $N_S = 30$). –We assume that the disorder distribution within each group ($\Delta_1, \Delta_2, \ldots, \Delta_{N_S}$) is *identical* across groups. This may seem a severe approximation, but it becomes less so as N_s increases, as discussed in the following.

In such a partitioned distribution, one can readily identify the *equivalent* segments (chromophores)—one in each group—as for example, the four shaded segments in Fig. 4. Since all the equivalent segments have the same value of site disorder Δ_n, we can take

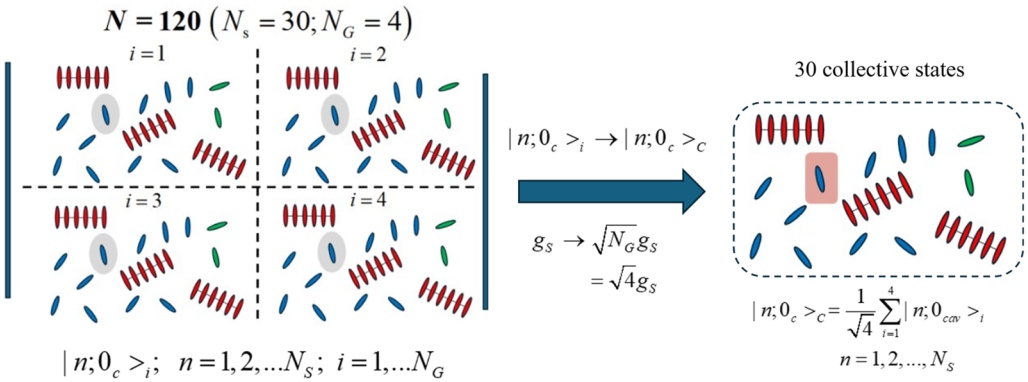

FIG. 4. Left panel: partitioning of an ensemble of $N = 120$ chromophore segments into four groups ($N_G = 4$), each containing $N_s = 30$ segments (two units) with the aggregate composition deduced from the absorption spectral analysis ($N_{agg} = 18$, $N_1 = 10$, and $N_2 = 2$). The disorder site energy distribution within each group ($\Delta_1, \Delta_2, \ldots, \Delta_{30}$) is assumed identical across groups. The local material excitation on the nth site in the ith group is denoted $|n;0_c\rangle_i$. Here, we consider the simpler case with no vibrations as described by a Tavis–Cummings Hamiltonian. An equivalent chromophore in each group is indicated with the shaded oval. Right panel: only the collective states, $|n;0_{cav}\rangle_C$, which are symmetric ($k = 0$) combinations of the equivalent molecules from each group, couple to the cavity field. The calculated reflectance spectrum (averaged over disorder configurations) becomes more accurate as the number of partitions N_G decreases (so that N_S increases) while maintaining $N = N_G N_S$. In reality, N is very large, in the range 10^7–10^{10}.

symmetric ($k = 0$) linear combinations of equivalent-segment excitations across N_G groups to define a *collective* basis set of matter-radiation states.[48] For example, a single-particle collective material state is given by

$$|n, \tilde{v}; 0_{cav}\rangle_C = \frac{1}{\sqrt{N_G}} \sum_{i=1}^{N_G} |n, \tilde{v}; 0_{cav}\rangle_i \,; n = 1, 2, \ldots N_S, \tag{11}$$

where $|n, \tilde{v}; 0_{cav}\rangle_i$ is the state where the nth segment of the ith group is vibronically excited with $\tilde{v}$ quanta ($\tilde{v} = 0, 1, 2 \ldots$) in the shifted ($S_1$) potential. Two-particle collective states are defined as

$$|n, \tilde{v}; m, v; 0_{cav}\rangle_C = \frac{1}{\sqrt{N_G}} \sum_{i=1}^{N_G} |n, \tilde{v}; m, v; 0_{cav}\rangle_i \,; n = 1, 2, \ldots N_s. \tag{12}$$

Here, $|n, \tilde{v}; m, v; 0_{cav}\rangle_i$ is the state where, within the ith group, the nth segment is vibronically excited, while the mth segment hosts a pure vibrational excitation with v (>0) vibrational quanta in the unshifted (S_0) ground state.

The collective states in Eqs. (11) and (12) are symmetric ($k = 0$) superpositions over excitations on *equivalent* segments within each group and, therefore, comprise a much smaller basis set than the complete basis set whenever $N_s \ll N$. If the sample size is assumed to be smaller than a cubic cavity-mode wavelength, then only such collective states will couple to the cavity field and therefore contribute to the cavity reflectivity, absorption and transmission spectra. This allows for a spectral simulation with a computationally manageable number of basis states. (In actual samples, the cavity thickness is of the order of λ/2 but the lateral dimension may exceed λ, requiring one to include small corrections due to nonzero k states.) As the number N_S increases—and the number of groups N_G decreases—the partition approximation becomes more accurate. In the limit of a single large group containing $N_s = N$ segments, the exact result is obtained. Fortunately, as we see in the following, convergence is achieved long before N_s becomes very large.

Finally, we consider the collective states containing a single cavity photon. The state with no electronic or vibrational excitations and one cavity photon is denoted as $|G;\ 1_{cav}\rangle$. There is only one such state, independent of the number of partitions, since G represents the vibrationless electronic ground state of all segments across all groups. There are also vibration-radiation states in which one or more molecules are vibrationally (but not electronically) excited.[32,40,41,48] The simplest such collective state hosts v vibrations on a single chromophore,

$$|g; 0_1, \ldots v_n, \ldots 0_{N_s}; 1_{cav}\rangle_C = \frac{1}{\sqrt{N_G}} \sum_{i=1}^{N_G} |g; 0_1, \ldots v_n, \ldots 0_{N_s}; 1_{cav}\rangle_i \,; \quad n = 1, 2, \ldots N_s, \tag{13}$$

where $|g; 0_1, \ldots v_n, \ldots 0_{N_s}; 1_{cav}\rangle_i$ is the state consisting of a single cavity photon and v vibrational quanta on the nth segment in the ith group. There are also collective states with two or more vibrations distributed over two or more chromophores; see Ref. 48.

After expressing the Hamiltonian in Eq. (10) in a reduced ($N_s \times N_s$) collective basis set, we invoke the simple ansatz described in Ref. 48, where all of the radiation–matter coupling terms involving radiation-vibration states with one or more vibrational quanta are scaled by an additional factor of $\sqrt{N_G}$. The resulting Hamiltonian then maps directly onto the Hamiltonian in Eq. (10) with $N = N_s$ segments, but with the radiation–matter coupling scaled by $\sqrt{N_G}$, i.e., with $g_S \to \sqrt{N_G} g_S$ (for details, see Ref. 48). The ansatz is quite intuitive: the reduction in basis set afforded by the collective basis set is offset by increasing the radiation–matter coupling to reflect the collective (delocalized) nature of each state.

In order to evaluate the cavity spectral response involving a large number N ($=N_s \times N_G$) of chromophore segments with a Gaussian distribution of segment-energy fluctuations, we adhere to the following algorithm. The value for the overall light–matter coupling, $\Omega \equiv \sqrt{N} g_S$, is first estimated from the spectral separation between the LP and UP in the measured P3HT spectrum, giving $\Omega \approx 1$ eV. We begin with the minimum value of $N_s = 15$ (one "unit")—and therefore a large number of $N_G = N/N_s$ groups—and generate a random configuration of disorder $\{\Delta_1, \Delta_2, \ldots, \Delta_{15}\}$, as described in Sec. II. After making the aforementioned ansatz,[48] the $N_s \times N_s$ Hamiltonian in the collective basis becomes equivalent to solving for the eigenstates of the Hamiltonian in Eq. (10) with $N = N_s$, but with the radiation-matter interaction g_s replaced by

$$\sqrt{N_G}\, g_s = \Omega/\sqrt{N_s} \approx 0.26 \text{ eV}$$

after inserting $N_s = 15$. After evaluating the reflectivity spectrum (as described in Sec. IV), we consider additional random configurations of disorder and compute the average reflectivity spectrum. This is conducted for as many configurations as are required for convergence, usually about 1000. Next, we increase N_s (decrease N_G) to include two or more units and repeat the entire process. In the limit that $N_s = N$ and $N_G = 1$ (which, of course, is not computationally feasible), the spectrum becomes exact, without any partitioning approximations. Hence, if we observe convergence of the reflectivity spectrum for much smaller values of N_s, we can be reasonably assured that our algorithm has delivered the desired goal—the reflectivity spectrum of the large ensemble of N segments.

Before considering the details surrounding the calculation of the reflectivity spectrum, we briefly point out that a distribution of randomly oriented dipoles is readily accounted for by simply renormalizing the light–matter coupling constant, g_s. Sommer *et al.*[36] showed that a distribution of randomly oriented in-plane transition dipoles can be mapped onto a system of aligned dipoles with a reduced radiation–matter coupling, g_s, by $\sqrt{2}$. Hence, we do not have to resort to a more complex two-mode Hamiltonian (two orthogonally polarized cavity modes) with randomly oriented segment distributions to account for an isotropic random distribution of P3HT segment dipoles. We simply consider a distribution of aligned segments with our single-mode Hamiltonian in Eq. (10), and reinterpret g_s to be have been renormalized to reflect an isotropic distribution of dipoles.

B. Reflectivity spectrum

In order to obtain the reflectivity spectrum, we follow the method introduced in Ref. 31, which is based on a Lindblad treatment of the various relaxation pathways available to the polariton

states $|\varepsilon_j\rangle$, obtained from the diagonalization of the FHTC Hamiltonian in Eq. (10). Accordingly, the system density matrix abides by the equation,

$$\frac{d}{dt}\hat{\rho} = -i[\hat{H}_{\mathrm{FHTC}} + V_p(t), \hat{\rho}] + \kappa \hat{L}_{\hat{a}}[\hat{\rho}] + \gamma_r \hat{L}_{\hat{\mu}}[\hat{\rho}] + \gamma_{nr}\sum_n \hat{L}_{\hat{\sigma}_n}[\hat{\rho}] + \gamma_{\mathrm{vib}}\sum_n \hat{L}_{\tilde{b}_n}[\hat{\rho}], \tag{14}$$

where $V_p(t) \propto \mathcal{E}e^{i\omega_p t} + h.c.$ is a time-dependent Hamiltonian representing the interaction with the coherent probe field at frequency ω_p, which weakly drives the cavity from the total ground state, $|G;\, 0_{cav}\rangle$. Equation (14) includes four relaxation terms; in order of appearance, they are (1) the decay rate κ due to radiation leakage through the mirrors, (2) the collective radiative decay rate γ_r, (3) the electronic nonradiative decay rate γ_{nr}, and finally, (4) the vibrational relaxation rate, γ_{vib}. All such terms are expressed in the form of a Lindbladian super-operator,[33]

$$\hat{L}_{\hat{O}}[\hat{\rho}] \equiv \hat{O}\hat{\rho}\hat{O}^{\dagger} - \frac{1}{2}(\hat{O}^{\dagger}\hat{O}\hat{\rho} + \hat{\rho}\hat{O}^{\dagger}\hat{O}). \tag{15}$$

As shown in Ref. 31, the solution of the Lindblad equation expressed in the eigenbasis of H_{FHTC}—here expanded to include vibrational relaxation at rate γ_{vib}—results in a decay rate Γ_j for the jth polariton, given by

$$\Gamma_j \equiv \kappa F_j^{cav} + \gamma_r F_j^{(r)} + \gamma_{nr} F_j^{(nr)} + \gamma_{\mathrm{vib}} F_j^{(vib)}, \tag{16}$$

where the relaxation due to cavity leakage, dipole radiation, nonradiative decay, and vibrational relaxation are governed by wave function component factors,

$$F_j^{(cav)} \equiv \sum_i |\langle \eta_i|\, \hat{a}\, |\varepsilon_j\rangle|^2, \tag{17a}$$

$$F_j^{(r)} \equiv \sum_i |\langle \eta_i|\, \hat{\mu}\, |\varepsilon_j\rangle|^2, \tag{17b}$$

$$F_j^{(nr)} \equiv \sum_i \sum_{n=1}^{N} |\langle \eta_i|\hat{\sigma}_n\, |\varepsilon_j\rangle|^2, \tag{17c}$$

$$F_j^{(vib)} \equiv \sum_{i(\neq j)} \sum_{n=1}^{N} |\langle \varepsilon_i|\tilde{b}_n\, |\varepsilon_j\rangle|^2, \tag{17d}$$

where $|\eta_i\rangle$ is the ith state within the ground-state electronic manifold with no photons, which includes the overall ground state,

$$|G;0_{\mathrm{vac}}\rangle \;=\; |g_1 0_1, g_2 0_2, \ldots, g_N 0_N; 0_{cav}\rangle \tag{18}$$

as well as purely vibrational excited states built upon $|G;0_{cav}\rangle$, for example, states with a single vibrational quantum of energy such as $|g_1 0_1, g_2 1_2, \ldots, g_N 0_N;\, 0_{cav}\rangle$, states with two vibrational quanta, $|g_1 0_1, g_2 1_2, g_3 1_3, \ldots, g_N 0_N;\, 0_{cav}\rangle$, and so on. We have also introduced the shifted annihilation operator of the vibrational field, $\tilde{b}_n \equiv \hat{b}_n + \lambda|n\rangle\langle n|$, ensuring the same decay rate exists between levels of the shifted and unshifted potential wells.

The expression for reflectivity is based on a solution of the Lindblad equation under the Born–Markov approximation and a second-order perturbation treatment for the probe field (for details, see Sec. S.3 in the supplementary material). Utilizing the energy flux conservation condition, $R + T + A = 1$, we obtain

$$R(\omega) = 1 - \sum_j \frac{\frac{\kappa}{2}|\langle G|\hat{a}\,|\varepsilon_j\rangle|^2}{(\omega - \omega_{Gj})^2 + \left(\frac{\Gamma_j}{2}\right)^2}\left\{\Gamma_j - \frac{\kappa}{2}F_j^{(cav)}\right\}. \tag{19}$$

Here, $\omega_{Gj} \equiv \varepsilon_j$ is the polariton transition frequency corresponding to the $|G;\, 0_{cav}\rangle \rightarrow |\varepsilon_j\rangle$ transition (taking the zero of energy to be that corresponding to the ground state $|G{:}0_{cav}\rangle$), obtained through direct diagonalization of H_{FHTC}. When site disorder is present, the spectrum in Eq. (19) is averaged over a sufficient number of disorder configurations to achieve convergence. For completeness, we provide expressions for $T(\omega)$ and $A(\omega)$ in the supplementary material.

Table II summarizes the various relaxation and cavity parameters relevant for the P3HT microcavity. Relaxation is almost entirely dominated by κ and γ_{vib}. The cavity decay rate of 130 meV derives directly from the measured linewidth of the resonances observed in an empty cavity[25] and dominates the relaxation processes. The ensemble superradiant decay rate, reported as $N\gamma_r$, is treated in a manner similar to the ensemble light–matter coupling $\sqrt{N}g_S$. In particular, within our partition scheme, we utilize the *collective* radiative decay rate, $N_G\gamma_r$, to account for the enhancement accompanying delocalization over N_G groups. Since $N_G\gamma_r = N\gamma_r/N_S$, we simply take the value of $N\gamma_r$ in Table II divided by N_S as the radiative decay rate to replace γ_r in Eq. (14). Note that in the limit that $N_G = 1$ ($N_S = N$), the rate $N_G\gamma_r$ becomes the actual single segment radiative decay rate. The value of $N\gamma_r = 8$ meV in Table II corresponds to a relaxation time of 0.5 ps. This may appear rather long since γ_r for a single segment should be of the order of a nanosecond, requiring N to be only 10^3 for $N\gamma_r$ to attain the value reported in the Table. However, superradiant enhancement by N corresponds to an idealized ensemble of ordered and aligned chromophores, which is certainly not the case in a realistic sample. Hence, the value of N in

TABLE II. Relaxation and cavity parameters for the simulations in Figs. 3 and 5–7.

Relaxation parameters (meV)				Cavity parameters (eV)	
κ	$N\gamma_r$	γ_{nr}	γ_{vib}	$\sqrt{N}g_S$	ω_c
Cavity decay rate	Superradiant decay rate	Nonradiative decay rate	Vibrational relaxation rate	Ensemble light–matter coupling	Cavity frequency
130	8	4	40	0.91	2.43

$N\gamma_r$ should be interpreted as an effective value. In addition, Wang and Hsu[71] have recently shown that the enhancement by N depends on the cavity detuning and other geometric parameters—in some cases of physical relevance, the enhancement levels off making the radiative rate far less than $N\gamma_r$.

The vibrational relaxation rate in Table II is consistent with measured values[72] and corresponds to a relaxation time of several hundred femtoseconds. The nonradiative rate of 1 meV (50 ps relaxation time) is typical of many organic chromophores. The simulated spectra are almost entirely governed by κ and γ_{vib}. (Setting $N\gamma_r$ and γ_{nr} to zero has minimal effect.) Finally, the cavity frequency in Table II corresponds to that used in Ref. 25, while the radiation–matter interaction is the value required to attain the measured Rabi splitting (see below).

C. Simulated P3HT reflectivity spectrum

Using the partition scheme described above with the reflectivity expression in Eq. (19), we can now test our convergence algorithm for the P3HT films characterized in Sec. II. The Hamiltonian in Eq. (10) is employed using the cavity parameters and relaxation rates listed in Table II and the aggregate/amorphous composition and energy parameters from Table I. We emphasize that the ensemble light–matter coupling, $\sqrt{N}g_S$ = 0.91 eV, is chosen so that the Rabi splitting determined from the converged reflectivity spectrum agrees with the measured Rabi splitting of ~1 eV. Figure 5(a) shows the simulated spectra as a function of the number of chromophore segments, N_S, in each group, with the *collective* polaritons obtained by diagonalizing the Hamiltonian in Eq. (10) represented in just the single-particle material basis set [Eq. (11)] as well as the radiation vibration states in Eq. (13). Note that, according to the partitioning scheme, for each value of N_S, g_s in Eq. (10) is replaced by 0.91 eV $/\sqrt{N_S}$. Throughout, the ratio 9:5:1 is maintained for the aggregate vs amorphous composition. As can be observed from the figure, the convergence is rapid, with little difference between the two largest values of N_S (60 and 90). Importantly, the positions and linewidths of the LP and UP as well as MP_1 and MP_2 spectral "dips" are all well reproduced relative to the measured spectrum (dashed curve). In addition, there is an array of intermediate gray states between the lower and upper polaritons responsible for nonunity reflectivity over the entire span of 1 eV. The main discrepancy between the measured and simulated spectra concerns the lower relative reflectivity in the UP region in the measured spectrum. This may be due to the frequency-dependent optical properties of the silver mirrors, where the measured absorbance increases with energy as one approaches the plasmon resonance at ~4 eV,[73] thereby leading to a reduction in reflectivity for the UP relative to the LP. The disparity in the measured vs simulated spectra may also be due to the presence of additional nearby cavity modes.[22,74,75]

If we expand the basis set to include the two-particle material states in Eq. (12) as well as vibration–photon states, where two chromophores are vibrationally excited, the number of segments, N_S, that can be handled computationally is significantly reduced. The maximum that can be treated numerically is N_S = 30. In order to obtain three plots (N_S = 10, 20 and 30) for testing convergence, we maintained a 6:3:1 composition ratio, slightly different from the 9:5:1 ratio determined in Sec. II. Figure 5(b) shows the simulated reflectivity spectra. As can be seen, convergence is even faster than observed in Fig. 5(a) and is achieved with only N_S = 30 chromophores.

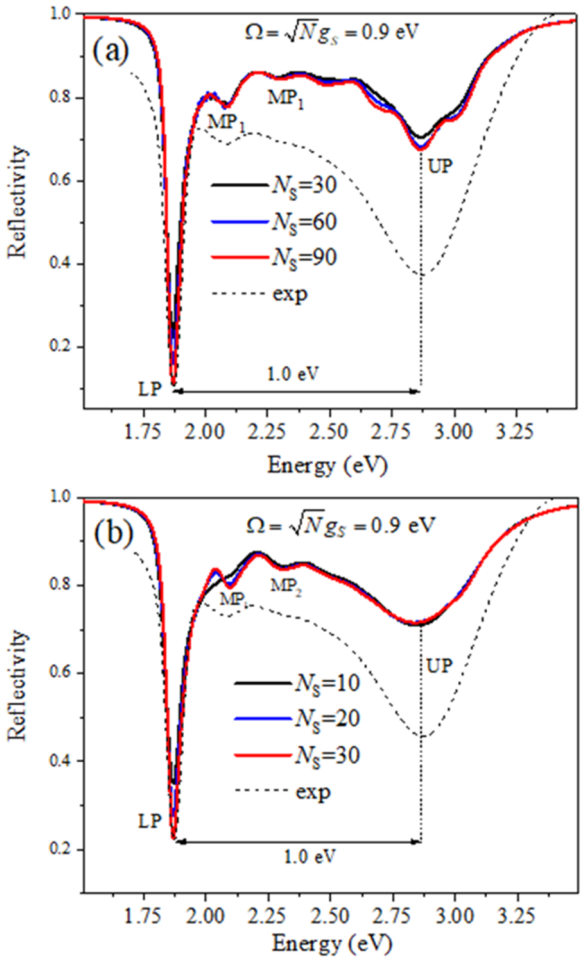

FIG. 5. Reflectivity spectra evaluated using Eq. (19) with the eigenstates and energies of the Hamiltonian in Eq. (10) represented in a basis set truncated at (a) the single-particle level and (b) the two-particle level. The energy parameters for the aggregate and amorphous regions are taken from Table I with the remaining parameters from Table II. In panel (a), the aggregate/amorphous composition ratio was held at 9:5:1 for the three values of N_S shown. In panel (b), the ratio was slightly different, 6:3:1, so that three curves could be obtained. The partitioning scheme was utilized with 500 configurations of disorder (see text). The dashed spectrum in panel (b) represents the measured spectrum from Ref. 25 normalized to the minimum reflectivity.

After gaining confidence with our partitioning algorithm, we turn to our best simulation for the P3HT film reflectivity, which is displayed in Fig. 3 alongside the measured spectrum. Here, we expressed the Hamiltonian in Eq. (10) parameterized as in Table II, in a collective basis set including all one and two-particle states for N_S = 30, maintaining the composition ratio 9:5:1 extracted from our free-space simulations, with the parameters listed in Table I. Overall, the positions and linewidths of all polaritons (LP, MP_1, MP_2, and UP) are well-captured, yielding excellent overall agreement with experiment. However, as in Fig. 5, the simulated UP reflectivity remains overestimated in comparison with the measured reflectivity.

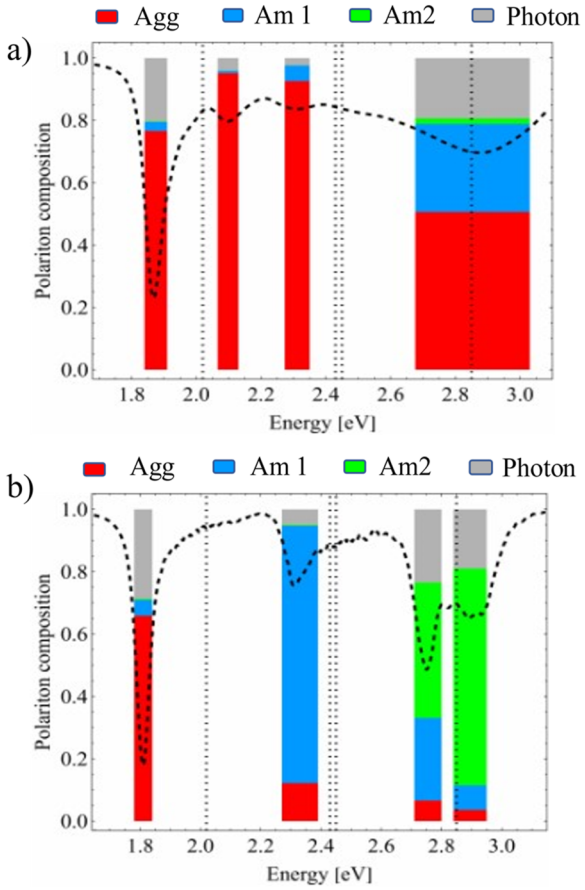

FIG. 6. (a) Composition of the four main polaritons evaluated according to Eq. (20) and based on the FHTC analysis, which yielded the best simulation in Fig. 3. The polariton component (Agg, Am1, Am2, and Photon) is proportional to the colored shaded region. Panel (b) is the same as panel (a), except after removing vibronic coupling (i.e., taking $\lambda = 0$). Vertical dashed lines in order of energy: aggregate 0-0 frequency (2.02 eV), cavity frequency (2.43 eV), Am1 0-0 frequency (2.45 eV), and Am2 0-0 frequency (2.85 eV).

In order to appreciate the nature of the polaritons responsible for the four main reflectivity "dips" in Figs. 3 and 5, we computed the average polariton composition within the spectral windows centered about each of the four dips; see Fig. 6(a). The mean composition for the states contributing to the non-unity reflectivity in the Ath window (A = LP, MP_1, MP_2, and UP) was obtained using the weighted average,

$$A_a = b\left\langle \sum_{j\,\epsilon\,\{A\}} (1 - R_j)a_j \right\rangle_C, \tag{20}$$

where A_a represents the contribution of the ath component (a = Agg, Am1, Am2, and cavity photon) to the Ath polariton. The sum is over all polaritons with energies lying within the Ath window, with the admixture of the ath component within the jth polariton represented by a_j (=$|\langle a|\varepsilon_j\rangle|^2$). The weighting factor 1-R_j (where R_j is the jth term in the sum in Eq. (19) evaluated at $\omega = \omega_{Gj}$) favors polaritons with the largest contribution to the reflectivity line shape. An average over all disorder distributions is indicated by $\langle\cdots\rangle_C$. Finally, the prefactor $b \equiv 1/\{\sum_a \langle \sum_{j\epsilon\{A\}} (1 - R_j)a_j\rangle_C\}$ ensures normalization, so that $\sum_a A_a = 1$.

Figure 6(a) shows the compositions of the dominant polariton states that contribute to the four spectral regions. The LP region is dominated by aggregate excitations, while the UP region, although also being dominated by aggregate excitations, contains a near equal Am1 component. The bias is due to the fact that the aggregate 0–0 energy (2.02 eV) is substantially smaller than the cavity photon frequency (2.43 eV), while the latter is near resonant with the Am1 0–0 energy (2.45 eV). The UP is not dominated by Am1 excitations because the number of aggregate segments is roughly double the number of Am1 segments. The photonic component is roughly 20% in both the LP and UP. The relatively small contribution relative to the material excitations arises from the substantial disorder present in the film. We have verified, for example, that when disorder is removed, the photonic contribution to the LP jumps to about 33%. If we further tuned the cavity photon frequency to the aggregate $k = 0$ exciton frequency, the photonic contribution becomes ~50%. By contrast, the middle polaritons contain very small photonic contributions of less than 5% (as expected from the reflectivity spectrum), but, similar to the LP, remain dominated by aggregate excitations.

Removing the vibronic coupling (by setting $\lambda = 0$) results in Fig. 6(b). In this case, the FHTC Hamiltonian is reduced to a Frenkel–Tavis–Cummings Hamiltonian. The spectrum and the polariton compositions are entirely different from that obtained with vibronic coupling [Fig. 6(a)]. Comparing Figs. 6(a) and 6(b) shows that vibronic coupling leads to a dramatic increase in the aggregate component to the middle and upper polaritons. This is likely due to the creation of higher-energy vibronic peaks in the aggregate absorption spectrum, which overlap the cavity photon frequency at ~2.4 eV, leading to more efficient aggregate-cavity coupling.

Figure 7(a) shows how the measured reflectivity spectrum responds to a change in the cavity frequency, as selected by the angle of incidence of the probe field. Figure 7(a) shows a selection of four measured reflectivity spectra for different angles of incidence, including the one used in Fig. 3, which corresponds to an angle of incidence of 10°. The blueshift of the LP and UP with increasing angle correlates with the change in angle of incidence from 10° to 68°. Notably, the UP undergoes a much greater blueshift than the LP, increasing the Rabi splitting to ~1.1 eV, while the MP_1 and MP_2 remain practically fixed.

Figure 7(b) shows the simulated reflectivities with the best match to the experimental spectra shown in Fig. 7(a). To determine the cavity frequency for each experimental angle of incidence, we use the simple cavity dispersion relation $\omega_c(\theta) = \omega_{c,0}\left(1 - \sin^2\theta/n^2\right)^{-1/2}$, which exhibits a monotonic increase as the angle grows between 0° and 90°. The assumed angle-independent refractive index of $n = 2.1$ results in the best fit and is close to the values reported in previous studies.[76,77] We stress here that the values found in the literature may be different to the case of P3HT films embedded in an optical cavity. The cavity energies resulting in the best agreement with the measured spectra for the incident angles considered in Fig. 7 are $\omega_c = 2.43$ eV (as reported in Table II for 10°), 2.5 eV(31°), 2.6 eV (50°), and 2.7 eV (68°), respectively.

In both the measured and simulated spectra, increasing ω_c results in the greatest dispersion for the UP. The four dashed lines

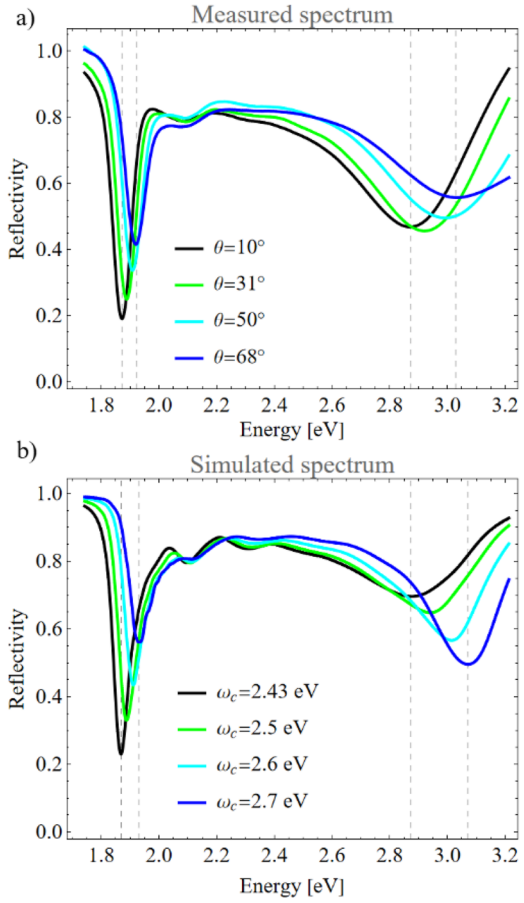

FIG. 7. (a) Measured reflectivity spectra for several values of the angle of incidence between the probe field wave vector and the cavity axis. (b) Simulated spectra for the cavity photon energies which correspond to the incidence angles in (a) (see text).

shown in Figs. 7(a) and 7(b) correspond to the positions of the LP and UP dips at 10° and 68°. For the measured spectra, the LP energy changes from 1.87 to 1.92 eV (1.87–1.93 eV, simulated) while the measured UP energy ranges from 2.87 to 3.03 eV (2.87–3.07 eV, simulated). Notably, both the measured and simulated spectra show that MP_1 and MP_2 remain almost fixed and independent of ω_c. As mentioned previously, we suspect that the disparity in the UP intensities between theory and experiment may be a result of the frequency-dependent optical properties of the silver mirrors,[73] which are neglected in our analysis.

To obtain some additional insight into the nature of the middle-polaritons, we show in Fig. 8 the reflectivity spectrum obtained for purely aggregated P3HT with $N_S = N_A = 30$. The remaining aggregate parameters are taken from Table I, and the cavity and relaxation parameters are taken from Table II. The spectrum is plotted alongside the simulated spectrum from Fig. 3. Since the value of $\sqrt{N}g_S$ is maintained at 0.91 eV in both spectra, they display similar Rabi splittings, although the LP and UP are redshifted from the composite spectrum due to the lack of the blueshifted amorphous

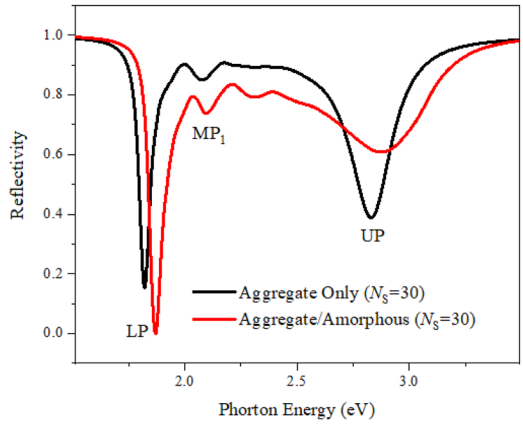

FIG. 8. Simulated reflectivity spectrum from Fig. 3 alongside the simulated spectrum for an aggregate-only sample.

chromophores. In addition, the UP for the aggregate-only composition is considerably narrower compared to the UP in the composite system, mainly due to the enhanced disorder widths of the amorphous vs aggregate domains (see Table I). Interestingly, the middle polaritons are present in both spectra and are fairly well-aligned, supporting their origin in the aggregate/amorphous mix as primarily from the aggregate component, consistent with Fig. 6. In particular, the position of MP_1 lies mid-way between ω_{0-0}^{Agg} and $\omega_{0-0}^{Agg} + \omega_{vib}$ and is approximately independent of the cavity frequency as noted earlier (see Figs. 6 and 7). Although not shown, the peaks positions are also practically unchanged when the disorder is removed.

We therefore investigated the possible origin of MP_1 as due to a Herzberg–Teller coupling mechanism, driven by vibronic coupling. Because of the near-invariance of the peak positions to disorder and cavity detuning, we consider the simplified case of disorder-free aggregates containing N segments, with the cavity tuned to the $k = 0$ exciton frequency. Because $\lambda^2\omega_{vib}$ is small compared to the Rabi splitting in P3HT microcavities, the vibronic coupling term in Eq. (6) is treated perturbatively. To zeroth order, the lower and upper polaritons can then be expressed in the polariton–phonon product basis,[41]

$$|LP(UP)\rangle \otimes |0_{q_1}, \ldots, 0_{q_N}\rangle, \tag{21a}$$

where the exciton–polaritons $|LP\rangle$ and $|UP\rangle$ are given by

$$|LP\rangle \equiv \frac{1}{\sqrt{2}}\{|k=0;0_{cav}\rangle - |g;1_{cav}\rangle\}, \tag{21b}$$

$$|UP\rangle \equiv \frac{1}{\sqrt{2}}\{|k=0;0_{cav}\rangle + |g;1_{cav}\rangle\}, \tag{21c}$$

and $|0_{q_1}, \ldots, 0_{q_N}\rangle$ is the phonon Fock state indicating zero phonons in each mode identified by its wave vector q (=0, $\pm 2\pi/N, \pm 4\pi/N \ldots \pi$). There is also a band of exciton–phonon states,

$$|k\rangle \otimes |1_q\rangle \otimes |0_{cav}\rangle \qquad k = \pm 2\pi/N, \pm 4\pi/N \ldots \pi, \tag{22}$$

where $|k\rangle$ is the "free" exciton wave vector and $|1_q\rangle$ is an abbreviated Fock state, indicating one phonon in the mode with wave

vector q and zero phonons in the remaining N-1 modes. (The k = 0 exciton is noticeably absent in Eq. (22) as it is involved in light–matter coupling to states like Eq. (21a) but with an additional phonon.) The exciton–phonon states in Eq. (22) have energies given by $\omega_{0-0}^{\mathrm{Agg}} + 2J_c \cos k + \omega_{\mathrm{vib}}$, which is in the vicinity of the MP_1 peak in Fig. 3, but cannot contribute to the reflectivity spectrum because the term $\langle G|\hat{a}\,|\varepsilon_j\rangle$ in Eq. (19) is zero. Such states can, however, mix with LP and UP polaritons in Eq. (21a) through the perturbation Hamiltonian, $H_{\text{ex-vib}}$, in Eq. (6) whenever the quasi-momentum, $k + q$, is zero (or 2π). In this manner, the exciton–phonon states "borrow" optical intensity from the LP and UP states in accord with the HT mechanism. Hence, the product states in Eq. (22) with $q = -k$ can be considered "bright" vibronic polaritons, with the remaining states ($q \neq -k$) being dark vibronic excitons, related to the dark vibronic polaritons introduced in Ref. 32.

In Sec. S.4 in the supplementary material, we analyze the Hamiltonian in Eq. (10), in much greater detail, treating the exciton–vibration coupling perturbatively (and maintaining no disorder). By correcting the exciton–phonon state in Eq. (22) to first order, it is shown (see Fig. S.3) how the absorption spectrum develops a broad spectral peak between $\omega_{0-0}^{\mathrm{Agg}} + \omega_{\mathrm{vib}} - 2J_C$ and $\omega_{0-0}^{\mathrm{Agg}} + \omega_{\mathrm{vib}} + 2J_C$, which effectively reproduces the exciton dispersion band due to intensity borrowing from like-symmetry LP and UP states. The analysis in the supplementary material further shows how, with increasing λ^2, the spectrum evolves into two distinct peaks, MP_1 and MP_2, which effectively "bracket" the broad perturbative peak, showing important effects beyond pertubation theory. In this regard, the peaks are fairly insensitive to the Coulomb coupling, as demonstrated in Fig. S.4.

IV. CONCLUSION

In this work, we presented a viable numerical approach for evaluating the microcavity reflectivity spectrum for a large ensemble of disordered organic chromophores, with direct application to the semicrystalline thin films of P3HT. An analysis of a thin film in free-space based on a Frenkel–Holstein Hamiltonian revealed the presence of both aggregate and amorphous domains, with energies differing by almost 0.5 eV in agreement with prior studies.[38,39] Subsequent application of the FHTC Hamiltonian for P3HT microcavities along with a partitioning scheme developed to treat large, disordered ensembles of chromophores yields a reflectivity spectrum in excellent agreement with experiment, reproducing not only the lower and upper polaritons but also the middle polaritons—or bright vibronic polaritons. The origin of the MP_1 reflectivity dip can be traced to exciton–phonon excitations with zero quasi-momentum—bright vibronic polaritons—made visible via Herzberg–Teller intensity borrowing from the lower and upper polaritons. Interestingly, the bright vibronic polaritons derive from free-space exciton–phonon product states with energies not too different from the polariton energies, in line with the gray-state description of George *et al.*[25] However, both the LP and UP possess energies quite distinct from the energies of their dominant bare exciton components; for example, the UP at an energy near 3 eV contains comparable contributions from aggregate and amorphous excitations. In future works, we will consider the photoluminescence spectrum obtained via high-energy, incoherent excitation in order to probe the *dark* vibronic polaritons.[32,41] Such quasi-particles have nonzero quasi-momentum, making them invisible in the reflectivity spectrum, but nevertheless appear in the photoluminescence spectrum via emission to the ground state with one or more vibrational quanta. We will also consider microcavities containing a wider array of organic chromophores, especially those which show a more pronounced vibronic progression in the free-space absorption spectrum and with less disorder—i.e., no amorphous regions. This will allow us to better investigate the robustness of our approach. Finally, it is relatively straightforward to adapt our approach to treat polariton dynamics,[15,18–22] which can be directed toward a more comprehensive understanding of energy transfer between aggregate and amorphous domains, similar to studies that explore energy transfer between different chromophores within a cavity.[11,12]

SUPPLEMENTARY MATERIAL

The supplementary material encompasses convergence of the aggregate absorption spectrum in free-space, a treatment of the Tavis–Cummings Hamiltonian in the ultra-strong coupling regime, a description of the Lindblad approach to evaluating relaxation and a perturbative treatment of the HTC Hamiltonian, and a demonstration of the insensitivity of the middle polaritons to Coulomb coupling.

ACKNOWLEDGMENTS

The work by H.H., M.A., F.C.S., A.G., and A.J.M. was supported by the Air Force Office of Scientific Research (AFOSR) under Award No. FA9550-23-1-0645. A.J.M. acknowledges support from the Alfred P. Sloan Foundation. F.H. was supported by ANID-Fondecyt Regular Grant No. 1221420 and Millennium Science Initiative Program No. ICN17_012. This research includes calculations carried out on HPC resources supported by the US Army Research Laboratory under Contract No. ARL W911NF212007.

AUTHOR DECLARATIONS

Conflict of Interest

The authors have no conflicts to disclose.

Author Contributions

Hamed Haghshenas: Formal analysis (equal); Investigation (equal). **Mauricio Arias**: Formal analysis (equal); Investigation (equal); Methodology (equal). **Aleesha George**: Data curation (lead); Investigation (supporting). **Andrew J. Musser**: Conceptualization (supporting); Funding acquisition (equal). **Felipe Herrera**: Conceptualization (equal); Investigation (supporting). **Frank C. Spano**: Conceptualization (lead); Funding acquisition (equal); Project administration (equal).

DATA AVAILABILITY

The data that support the findings of this study are available from the corresponding author upon reasonable request.

REFERENCES

[1] W. Ahn *et al.*, "Modification of ground-state chemical reactivity via light–matter coherence in infrared cavities," Science **380**(6650), 1165–1168 (2023).

[2]J. Yuen-Zhou and V. M. Menon, "Polariton chemistry: Thinking inside the (photon) box," Proc. Natl. Acad. Sci. U. S. A. **116**(12), 5214–5216 (2019).
[3]R. F. Ribeiro *et al.*, "Polariton chemistry: Controlling molecular dynamics with optical cavities," Chem. Sci. **9**(30), 6325–6339 (2018).
[4]T. W. Ebbesen, "Hybrid light–matter states in a molecular and material science perspective," Acc. Chem. Res. **49**(11), 2403–2412 (2016).
[5]A. D. Dunkelberger *et al.*, "Vibration-cavity polariton chemistry and dynamics," Annu. Rev. Phys. Chem. **73**, 429–451 (2022).
[6]F. J. Garcia-Vidal, C. Ciuti, and T. W. Ebbesen, "Manipulating matter by strong coupling to vacuum fields," Science **373**(6551), eabd0336 (2021).
[7]J. Feist, J. Galego, and F. J. Garcia-Vidal, "Polaritonic chemistry with organic molecules," ACS Photonics **5**(1), 205–216 (2018).
[8]B. S. Simpkins, A. D. Dunkelberger, and I. Vurgaftman, "Control, modulation, and analytical descriptions of vibrational strong coupling," Chem. Rev. **123**(8), 5020–5048 (2023).
[9]T. E. Li *et al.*, "Molecular polaritonics: Chemical dynamics under strong light–matter coupling," Annu. Rev. Phys. Chem. **73**, 43–71 (2022).
[10]J. Flick *et al.*, "Atoms and molecules in cavities, from weak to strong coupling in quantum-electrodynamics (QED) chemistry," Proc. Natl. Acad. Sci. U. S. A. **114**(12), 3026–3034 (2017).
[11]K. Georgiou *et al.*, "Ultralong-range polariton-assisted energy transfer in organic microcavities," Angew. Chem. **133**(30), 16797–16803 (2021).
[12]D. M. Coles *et al.*, "Polariton-mediated energy transfer between organic dyes in a strongly coupled optical microcavity," Nat. Mater. **13**(7), 712–719 (2014).
[13]P. Andrew and W. L. Barnes, "Förster energy transfer in an optical microcavity," Science **290**(5492), 785–788 (2000).
[14]W. Ying *et al.*, "Microscopic theory of polariton group velocity renormalization," Nat. Commun. **16**(1), 6950 (2025).
[15]G. Sandik *et al.*, "Cavity-enhanced energy transport in molecular systems," Nat. Mater. **24**, 344–355 (2024).
[16]M. Balasubrahmaniyam *et al.*, "From enhanced diffusion to ultrafast ballistic motion of hybrid light–matter excitations," Nat. Mater. **22**(3), 338–344 (2023).
[17]S. Hou *et al.*, "Ultralong-range energy transport in a disordered organic semiconductor at room temperature via coherent exciton–polariton propagation," Adv. Mater. **32**(28), 2002127 (2020).
[18]F. Wu *et al.*, "Efficient cavity-mediated energy transfer between photosynthetic light harvesting complexes from strong to weak coupling regime," Nat. Commun. **16**(1), 5300 (2025).
[19]M. Du *et al.*, "Theory for polariton-assisted remote energy transfer," Chem. Sci. **9**(32), 6659–6669 (2018).
[20]D. J. Tibben *et al.*, "Molecular energy transfer under the strong light–matter interaction regime," Chem. Rev. **123**(13), 8044–8068 (2023).
[21]Y.-C. Wei *et al.*, "Can nanocavities significantly enhance resonance energy transfer in a single donor–acceptor pair?," J. Phys. Chem. C **125**(33), 18119–18128 (2021).
[22]R. F. Ribeiro, "Multimode polariton effects on molecular energy transport and spectral fluctuations," Commun. Chem. **5**(1), 48 (2022).
[23]C. A. DelPo *et al.*, "Polariton decay in donor–acceptor cavity systems," J. Phys. Chem. Lett. **12**(40), 9774–9782 (2021).
[24]V. N. Peters *et al.*, "Effect of strong coupling on photodegradation of the semiconducting polymer P3HT," Optica **6**(3), 318–325 (2019).
[25]A. George *et al.*, "Controlling the manifold of polariton states through molecular disorder," Adv. Opt. Mater. **12**(11), 2302387 (2024).
[26]H. Sirringhaus *et al.*, "Two-dimensional charge transport in self-organized, high-mobility conjugated polymers," Nature **401**, 685 (1999).
[27]B. Balraj *et al.*, "A critical review on decade progress and future prospects of P3HT:PCBM bulk heterojunction solar cells," Sol. Energy **297**, 113574 (2025).
[28]A. Frisk Kockum *et al.*, "Ultrastrong coupling between light and matter," Nat. Rev. Phys. **1**(1), 19–40 (2019).
[29]J. Dubail *et al.*, "Large random arrowhead matrices: Multifractality, semilocalization, and protected transport in disordered quantum spins coupled to a cavity," Phys. Rev. A **105**(2), 023714 (2022).
[30]F. Herrera and W. L. Barnes, "Multiple interacting photonic modes in strongly coupled organic microcavities," Philos. Trans. R. Soc. A **382**(2287), 20230343 (2024).
[31]F. Herrera and F. C. Spano, "Absorption and photoluminescence in organic cavity QED," Phys. Rev. A **95**(5), 053867 (2017).
[32]F. Herrera and F. C. Spano, "Dark vibronic polaritons and the spectroscopy of organic microcavities," Phys. Rev. Lett. **118**(22), 223601 (2017).
[33]N. Shammah *et al.*, "Superradiance with local phase-breaking effects," Phys. Rev. A **96**(2), 023863 (2017).
[34]N. Wu, J. Feist, and F. J. Garcia-Vidal, "When polarons meet polaritons: Exciton-vibration interactions in organic molecules strongly coupled to confined light fields," Phys. Rev. B **94**(19), 195409 (2016).
[35]J. Liu, Q. Zhao, and N. Wu, "Vibration-assisted exciton transfer in molecular aggregates strongly coupled to confined light fields," J. Chem. Phys. **150**(10), 105102 (2019).
[36]C. Sommer *et al.*, "Molecular polaritonics in dense mesoscopic disordered ensembles," Phys. Rev. Res. **3**(3), 033141 (2021).
[37]F. C. Spano, "Optical microcavities enhance the exciton coherence length and eliminate vibronic coupling in J-aggregates," J. Chem. Phys. **142**(18), 184707 (2015).
[38]J. Clark *et al.*, "Determining exciton bandwidth and film microstructure in polythiophene films using linear absorption spectroscopy," Appl. Phys. Lett. **94**(16), 163306 (2009).
[39]J. Clark *et al.*, "Role of intermolecular coupling in the photophysics of disordered organic semiconductors: Aggregate emission in regioregular polythiophene," Phys. Rev. Lett. **98**(20), 206406 (2007).
[40]F. Herrera and F. C. Spano, "Cavity-controlled chemistry in molecular ensembles," Phys. Rev. Lett. **116**(23), 238301 (2016).
[41]F. Herrera and F. C. Spano, "Theory of nanoscale organic cavities: The essential role of vibration-photon dressed states," ACS Photonics **5**(1), 65–79 (2018).
[42]M. E. Mondal *et al.*, "Polariton spectra under the collective coupling regime. I. Efficient simulation of linear spectra and quantum dynamics," J. Chem. Phys. **162**(1), 014114 (2025).
[43]W. Ying, M. E. Mondal, and P. Huo, "Theory and quantum dynamics simulations of exciton-polariton motional narrowing," J. Chem. Phys. **161**(6), 064105 (2024).
[44]M. A. Zeb, P. G. Kirton, and J. Keeling, "Exact states and spectra of vibrationally dressed polaritons," ACS Photonics **5**(1), 249–257 (2018).
[45]F. C. Spano, "Absorption in regio-regular poly(3-hexyl)thiophene thin films: Fermi resonances, interband coupling and disorder," Chem. Phys. **325**, 22–35 (2006).
[46]F. C. Spano, "Modeling disorder in polymer aggregates: The optical spectroscopy of regioregular poly(3-hexylthiophene) thin films," J. Chem. Phys. **122**, 234701 (2005).
[47]F. C. Spano and C. Silva, "H- and J-aggregate behavior in polymeric semiconductors," Annu. Rev. Phys. Chem. **65**, 477–500 (2014).
[48]F. C. Spano, "Exciton–phonon polaritons in organic microcavities: Testing a simple ansatz for treating a large number of chromophores," J. Chem. Phys. **152**(20), 204113 (2020).
[49]J. B. Pérez-Sánchez *et al.*, "Simulating molecular polaritons in the collective regime using few-molecule models," Proc. Natl. Acad. Sci. U. S. A. **120**(15), e2219223120 (2023).
[50]H. Zoubi and G. La Rocca, "Microscopic theory of anisotropic organic cavity exciton polaritons," Phys. Rev. B **71**(23), 235316 (2005).
[51]J. del Pino, J. Feist, and F. J. Garcia-Vidal, "Quantum theory of collective strong coupling of molecular vibrations with a microcavity mode," New J. Phys. **17**(5), 053040 (2015).
[52]M. S. Skolnick, T. A. Fisher, and D. M. Whittaker, "Strong coupling phenomena in quantum microcavity structures," Semicond. Sci. Technol. **13**(7), 645 (1998).
[53]T. E. Li, A. Nitzan, and J. E. Subotnik, "Cavity molecular dynamics simulations of vibrational polariton-enhanced molecular nonlinear absorption," J. Chem. Phys. **154**(9), 094124 (2021).
[54]A. Mandal *et al.*, "Theoretical advances in polariton chemistry and molecular cavity quantum electrodynamics," Chem. Rev. **123**(16), 9786–9879 (2023).
[55]J. B. Pérez-Sánchez *et al.*, "CUT-E as a $1/N$ expansion for multiscale molecular polariton dynamics," J. Chem. Phys. **162**(6), 064101 (2025).
[56]J. Román-Roche *et al.*, "Linear response theory for cavity QED materials at arbitrary light–matter coupling strengths," Phys. Rev. B **111**(3), 035156 (2025).

[57]C.-Y. Cheng *et al.*, "Molecular polariton electroabsorption," Nat. Commun. **13**(1), 7937 (2022).
[58]M. S. Rider and W. L. Barnes, "Something from nothing: Linking molecules with virtual light," Contemp. Phys. **62**(4), 217–232 (2021).
[59]C. W. Gardiner and M. J. Collett, "Input and output in damped quantum systems: Quantum stochastic differential equations and the master equation," Phys. Rev. A **31**(6), 3761 (1985).
[60]C. Ciuti, G. Bastard, and I. Carusotto, "Quantum vacuum properties of the intersubband cavity polariton field," Phys. Rev. B **72**(11), 115303 (2005).
[61]J. A. Ćwik *et al.*, "Excitonic spectral features in strongly coupled organic polaritons," Phys. Rev. A **93**(3), 033840 (2016).
[62]J. Yuen-Zhou and A. Koner, "Linear response of molecular polaritons," J. Chem. Phys. **160**(15), 154107 (2024).
[63]H. J. Carmichael, *Statistical Methods in Quantum Optics 1: Master Equations and Fokker-Planck Equations* (Springer Science & Business Media, 2013).
[64]G. J. Small, "Herzberg–Teller vibronic coupling and the Duschinsky effect," J. Chem. Phys. **54**(8), 3300–3306 (1971).
[65]M. Wykes *et al.*, "Vibronic coupling in molecular crystals: A Franck-Condon Herzberg-Teller model of H-aggregate fluorescence based on quantum chemical cluster calculations," J. Chem. Phys. **143**(11), 114116 (2015).
[66]E. O. Odewale, A. G. Avramenko, and A. S. Rury, "Deciphering between enhanced light emission and absorption in multi-mode porphyrin cavity polariton samples," Nanophotonics **13**(14), 2695–2706 (2024).
[67]A. G. Avramenko and A. S. Rury, "Light emission from vibronic polaritons in coupled metalloporphyrin-multimode cavity systems," J. Phys. Chem. Lett. **13**(18), 4036–4045 (2022).
[68]M. Brinkmann, "Structure and morphology control in thin films of regioregular poly(3-hexylthiophene)," J. Polym. Sci., Part B: Polym. Phys. **49**, 1218–1233 (2011).
[69]M. R. Philpott, "Theory of the coupling of electronic and vibrational excitations in molecular crystals and helical polymers," J. Chem. Phys. **55**, 2039–2054 (1971).
[70]K. Schwennicke, N. C. Giebink, and J. Yuen-Zhou, "Extracting accurate light–matter couplings from disordered polaritons," Nanophotonics **13**(14), 2469–2478 (2024).
[71]S. Wang and L.-Y. Hsu, "Exploring superradiance effects of molecular emitters coupled with cavity photons and plasmon polaritons: A perspective from macroscopic quantum electrodynamics," J. Phys. Chem. C **127**(27), 12904–12912 (2023).
[72]N. Banerji *et al.*, "Ultrafast relaxation of the poly(3-hexylthiophene) emission spectrum," J. Phys. Chem. C **115**(19), 9726–9739 (2011).
[73]R. Hong *et al.*, "Surface-enhanced Raman scattering of silver thin films on as-roughened substrate by reactive ion etching," Appl. Phys. A **122**(3), 178 (2016).
[74]K. S. Menghrajani *et al.*, "Molecular strong coupling and cavity finesse," J. Phys. Chem. Lett. **15**(29), 7449–7457 (2024).
[75]M. S. Rider *et al.*, "Theory of strong coupling between molecules and surface plasmons on a grating," Nanophotonics **11**(16), 3695–3708 (2022).
[76]L. Hrostea, M. Girtan, R. Mallet, and L. Leontie, "Optical and morphological properties of P3HT and P3HT: PCBM thin films used in photovoltaic applications," IOP Conf. Ser.: Mater. Sci. Eng. **374**, 012015 (2018).
[77]L. Velasco Davoise, R. Peña Capilla, and A. M. Díez-Pascual, "Assessment of the refractive index and extinction coefficient of graphene-poly (3-hexylthiophene) nanocomposites," Polymers **14**(9), 1828 (2022).